Available online at www.sciencedirect.com

ScienceDirect

Ceramics International 39 (2013) 9435–9445

CERAMICS INTERNATIONAL

www.elsevier.com/locate/ceramint

Synthesis and characterization of $Ni_{0.8}Co_{0.2}Fe_2O_4$–$Ba_{0.95}Sr_{0.05}TiO_3$ multiferroic composites

Poonam Pahuja[a], Richa Sharma[a], Chandra Prakash[b], R.P. Tandon[a,*]

[a]Department of Physics and Astrophysics, University of Delhi, Delhi 110007, India
[b]Solid State Physics Laboratory, Timarpur, Delhi 110054, India

Received 7 March 2013; received in revised form 28 April 2013; accepted 10 May 2013
Available online 23 May 2013

Abstract

In this paper, structural, microstructural, dielectric, magnetic, ferroelectric, and magnetoelectric properties of a multiferroic composite with compositional formula (x) $Ni_{0.8}Co_{0.2}Fe_2O_4$+(1−x) $Ba_{0.95}Sr_{0.05}TiO_3$ (where x=0.0, 0.02, 0.04, 0.06, 0.08, 0.10, 1.00) has been studied. Nanoparticles of $Ni_{0.8}Co_{0.2}Fe_2O_4$ ferrite have been prepared by the sol–gel method. $Ba_{0.95}Sr_{0.05}TiO_3$ ceramic, synthesized by solid state reaction, has particle size in the micrometer range. X-ray analysis along with Rietveld refinement confirmed the formation of cubic spinel and perovskite structure for ferrite and ferroelectric phases, respectively. Transmission Electron Microscopy (TEM) analysis showed that $Ni_{0.8}Co_{0.2}Fe_2O_4$ particles have particle size in 25–60 nm range. Samples were characterized for the microstructural analysis by Scanning Electron Microscopy (SEM). Quantitative elemental analysis of the composite samples was carried out by Energy Dispersive X-ray Spectroscopy (EDS). Dielectric properties were studied as a function of frequency in the range 20 Hz–1 MHz for pure and composite samples. AC conductivity measurements suggested that small polaron hopping is the dominant conduction mechanism in the composites. Polarization vs. Electric field (P–E) and Magnetization vs. Magnetic field (M–H) hysteresis loop measurements respectively, confirmed good ferroelectric and ferromagnetic behavior of the composites. Complex impedance spectroscopy measurements at different temperatures confirmed the semiconducting nature of the composites. Magnetoelectric coupling between ferrite and ferroelectric phases was confirmed by measuring M–H hysteresis loops of electrically poled and unpoled samples.

Keywords: A. Sol–gel processes; B. Grain boundaries; C. Dielectric properties; C. Ferroelectric properties

1. Introduction

Multiferroics are the materials with ferroelectric and ferromagnetic orders coexisting and exhibiting coupling between magnetic and electric fields [1]. These materials become polarized when placed in magnetic field and get magnetized when placed in electric field [2,3]. Multiferroic materials find potential applications in filters, actuators, switches, transformers, multilayered capacitors, memory devices, transducers, phase shifters, magnetic field sensors, microwave devices, etc. [1,4–7]. Multiferroic materials can essentially be divided into two types: single phase and the composite materials [5,8]. The use of single phase multiferroic materials is limited due to their low magnetoelectric (ME) output [9]. In the composites, ME effect appears as the product property. In the present study, the composites consist of a suitable combination of piezoelectric and piezomagnetic phases [4]. The basic mechanism involved in these composites is that applied electric field produces strain in lattice due to piezoelectricity, which passes to piezomagnetic phase, and resulting in the generation of magnetic field through magnetostriction. Hence for high ME output, ferroelectric and ferromagnetic components should have high piezoelectric and magnetostrictive coefficients, respectively.

In the present work, $Ba_{0.95}Sr_{0.05}TiO_3$ (BST) has been selected as ferroelectric component due to its high dielectric constant, low dielectric loss, good thermal stability, high tunability, high breakdown strength, low leakage current density and high piezoelectric coefficient [10]. $Ni_{0.8}Co_{0.2}Fe_2O_4$ (NCF) has been chosen as ferromagnetic phase due to

*Corresponding author. Tel.: +91 11 27667725x1367; fax: +91 11 27667061.
E-mail addresses: ram_tandon@hotmail.com, rptandon9@physics.du.ac.in (R.P. Tandon).

0272-8842/$ - see front matter © 2013 Elsevier Ltd and Techna Group S.r.l. All rights reserved.
http://dx.doi.org/10.1016/j.ceramint.2013.05.061

its high electrical resistivity, high Curie temperature, high magnetostrictive coefficient, low eddy current losses, low losses at high frequencies, high saturation magnetization, environmental stability and low cost [11]. In this work, a multiferroic composite has been prepared with BST rich phase by keeping low content of NCF (only 2–10 wt%) since high ferrite concentration results in

1) Open (leaky) *P–E* loops even at high electric field strength due to high conductivity of ferrite phase, heterogeneous conduction, and interfacial polarization between ferrite and ferroelectric interfaces [12].
2) Less effective poling of the composite samples [13] resulting into lowering of piezoelectric coefficient for ferroelectric phase. This contributed to low magnetoelectric coefficient [14].

2. Experimental procedure

Nanoparticles of $Ni_{0.8}Co_{0.2}Fe_2O_4$ (NCF) were prepared by the sol–gel technique. Analytical grade ferric nitrate ($Fe(NO_3)_3 \cdot 9H_2O$), cobalt nitrate ($Co(NO_3)_2 \cdot 6H_2O$) and nickel nitrate ($Ni(NO_3)_2 \cdot 6H_2O$) were used as the starting materials. Ethanol and distilled water were employed as solvents. Nickel nitrate, cobalt nitrate and ferric nitrate were added in molar ratios of 0.8:0.2:2 in a mixture of solvents. The resulting solution was stirred vigorously for 8 h using a magnetic stirrer to obtain the sol. This sol was kept in oven at 60 °C for 24 h yielding a brown colored gel. This gel was dried at 120 °C for 12 h. The dried powder thus obtained was calcined in the temperature range 800–1000 °C for 6 h. Single phase NCF was formed at 950 °C. $Ba_{0.95}Sr_{0.05}TiO_3$ (BST) was prepared by solid state reaction using analytical grade barium carbonate ($BaCO_3$), strontium carbonate ($SrCO_3$) and titanium dioxide (TiO_2) as the starting materials. These starting powders were mixed in distilled water using zirconia balls for 24 h. The slurry thus obtained, was dried in an oven at 120 °C for 24 h. The dried mixture was ground using a mortar-pestle and calcined at 1050 °C for 6 h. The magnetoelectric (ME) composites were synthesized by mixing NCF and BST powders as per compositional formula (x) $Ni_{0.8}Co_{0.2}Fe_2O_4$+(1−x) $Ba_{0.95}Sr_{0.05}TiO_3$ (where x=0.00, 0.02, 0.04, 0.06, 0.08, and 0.10) using a ball mill and acetone as liquid medium for 12 h. BST and NCF powders may react together, during high temperature sintering process, leading to low magnetoelectric coupling [15]. In order to ensure whether these two constituents react or not, dried powder was calcined at 1050 °C for 6 h. XRD analysis of thus obtained calcined samples (not shown here) confirmed the presence of ferrite and ferroelectric phases only indicating that no chemical reaction took place between the two phases. The composite samples with x=0.0, 0.02, 0.04, 0.06, 0.08, 0.10, and 1.00 will hereafter be represented by S0, S2, S4, S6, S8, S10 and SN, respectively. The composite powder was pressed into pellets of diameter 13 mm and thickness 3–4 mm using polyvinyl alcohol (PVA) as binder. These pellets were sintered at 1250 °C in a box furnace for 6 h. Sintering temperature of pure NCF was optimized and found to be 1200 °C. Sintered pellets were lapped to ∼1 mm thickness using silicon carbide abrasive powder and then cleaned using an ultrasonicator. Phase identification of samples was performed with X-ray diffraction (XRD) technique using a Rigaku Miniflex II (Cu Kα radiation having λ=1.5406Å). The morphology and particle size of BST and NCF particles were examined using Transmission Electron Microscopy (TEM) (FEI Technai G^2T30). Microstructure of the composite samples was observed using Scanning Electron Microscopy (SEM) (Zeiss, MA15) having Energy Dispersive X-ray Spectroscopy (EDS) attachment. Silver paste was applied on both faces of pellets for making electrical contacts followed by annealing at 150 °C. Dielectric properties were measured as a function of frequency (20 Hz–1 MHz) at 30 °C using impedance analyzer (Wayne Kerr 6500B). Polarization versus electric field (*P–E*) hysteresis loops were recorded using an automated *P–E* loop tracer based on Sawyer-Tower circuit. Magnetic properties were studied using a Vibrating Sample Magnetometer (VSM).

3. Results and discussion

3.1. X-ray analysis

Fig. 1 shows XRD pattern of NCF, which clearly indicates the formation of single phase material with cubic spinel structure. Fig. 2(a) presents XRD patterns of pure BST and composite samples. The XRD analysis confirms the formation of cubic spinel structure of ferrite phase and tetragonal perovskite structure of ferroelectric phase in the composites. Absence of any extra peak in the XRD pattern indicates that no chemical reaction occurred between the two constituents of the composites during high temperature heat treatment. It can be

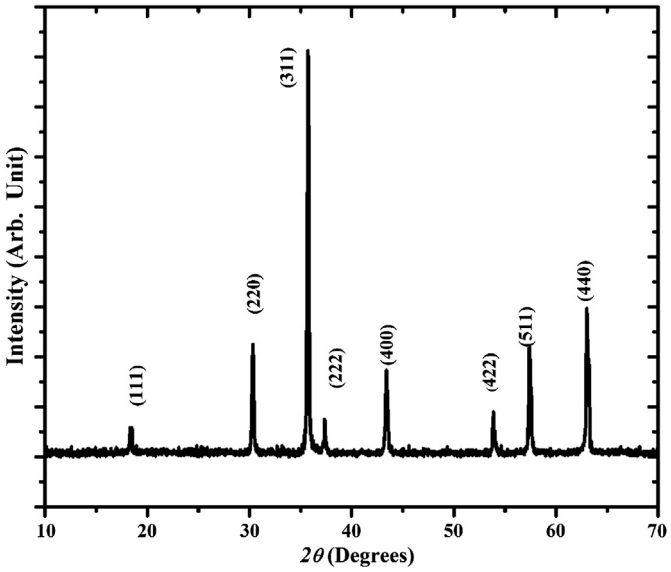

Fig. 1. XRD pattern of $Ni_{0.8}Co_{0.2}Fe_2O_4$.

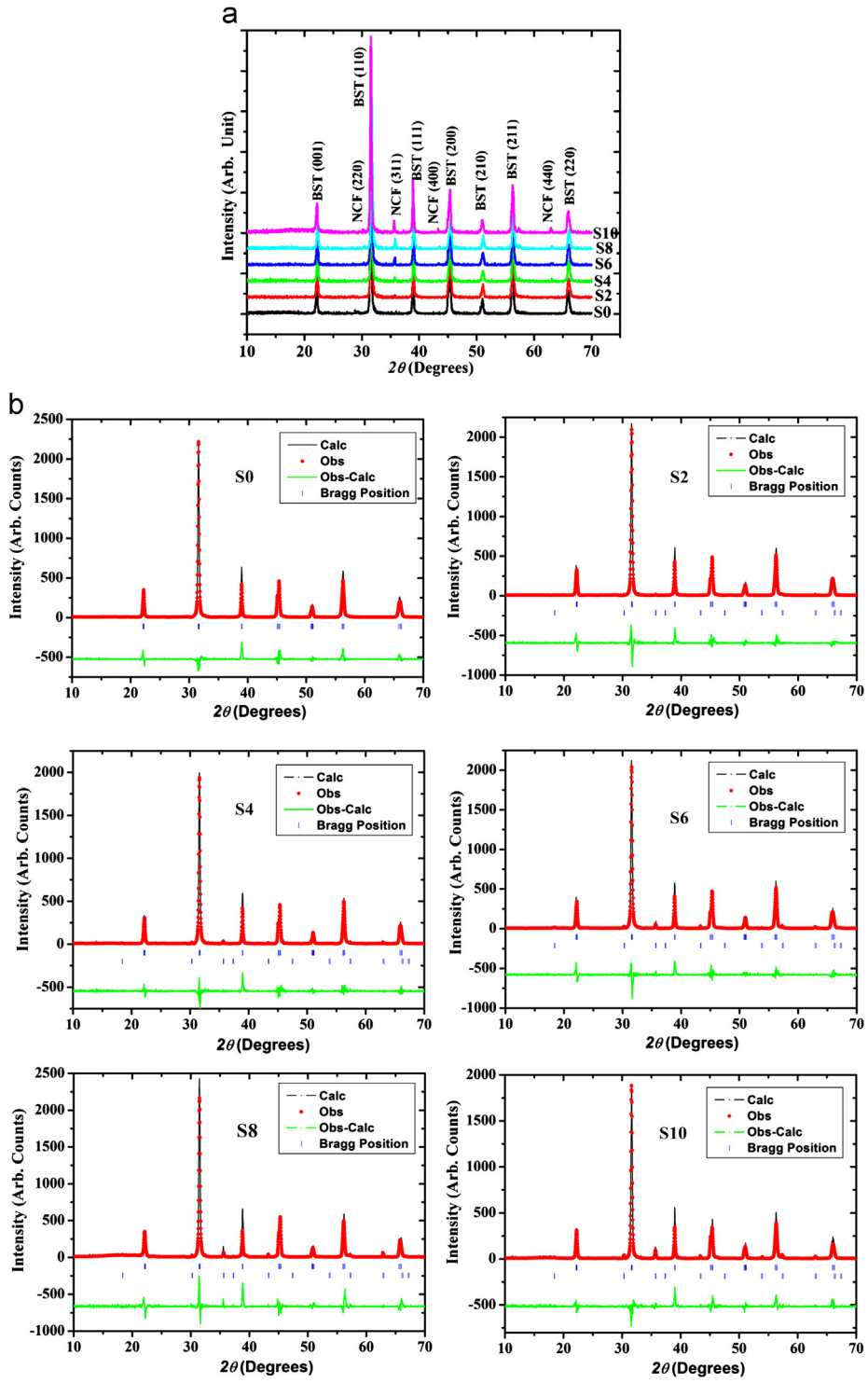

Fig. 2. (a) XRD pattern of $Ba_{0.95}Sr_{0.05}TiO_3$ and composite samples. (b) Rietveld refined XRD patterns of pure BST and composite samples where Obs and Calc represent observed and calculated data respectively.

noticed from the XRD pattern that intensity of ferrite peaks increases with increase in ferrite content. Rietveld refinement of the XRD data for pure BST and composite samples is carried out in two phase model using software FULLPROF. Fig. 2(b) shows the theoretical and experimental diffraction patterns of pure BST S0 and composite samples S2, S4, S6, S8 and S10. The structure of composites was refined in space group P4mm for ferroelectric phase and Fd-3m for ferrite phase. In Rietveld analysis, XRD data is refined by minimizing the difference between the observed and simulated powder diffraction patterns. This minimization is carried out by using mainly three reliability index parameters discrepancy factor

(R_{wp}), expected value (R_{exp}) and goodness of fit index (χ^2) which can be defined as [16,17]

$$R_{wp} = [(\sum_i wi(I_0 - I_c)^2)/(\sum_i wi I_0^2)]^{1/2}$$
$$R_{exp} = [(N-P)/(\sum_i wi I_0^2)]^{1/2}$$
$$\chi 2 = [R_{wp}/R_{exp}]^2$$

where I_0 and I_c are the experimental and calculated intensities, $wi=(1/I_0)$ and N are the weight and number of experimental observations and P is the number of fitting parameters. The values of these parameters along with structure refined lattice parameters for ferrite and ferroelectric phases, experimental density, X-ray density, relative density and porosity are listed in Table 1. Although R_{wp} values are slightly higher, still there is a good agreement between observed and simulated patterns. This may be attributed to

i. Out of the three reliability index parameters (R_{wp}, R_{exp}, $\chi 2$), $\chi 2$ is the main factor deciding the goodness of fit. Values of $\chi 2$ in the present case are reasonably small resulting in better fitting. Similar results can be seen in other reports [16,18,19].
ii. Rietveld refinement of the XRD data of the composite samples was carried out in two phase model. Rietveld refinement of XRD data in two phase model is a complex analysis in which refinement is carried out keeping in view space groups of both constituent phases, simultaneously involving a large number of varied parameters. This may result into a large value of R_{wp}.

The experimental density (ρ_e) of sintered pellets is determined using the Archimedes principle. Factors such as sintering conditions and sintering temperature affect ρ_e strongly.

X-ray density (ρ_x) is determined from the refined lattice parameters using the relation [20]

$$\rho_x = ZM/N_a a^3 \quad (1)$$

where Z is the number of molecules in the unit cell, M is molecular weight of the samples, N_a is Avogradro's Number and a is the lattice parameter.

Relative density (ρ_r) of the samples was calculated using the relation

$$\rho_r = \rho_e/\rho_x \quad (2)$$

The porosity (P) of the samples was calculated using the relation [20]

$$P = 1-\rho_r \quad (3)$$

Variation in the density of the composite samples from S0 to S10 may be explained in terms of three different factors

1) There are two opposing processes affecting the porosity of composite samples
   a) Filling of pores between BST grains by NCF nanoparticles
   b) Optimized sintering temperature for pure BST and NCF was 1250 °C and 1200 °C respectively. All the composite samples were sintered at 1250 °C, leading to over sintering of NCF due to its finer particle size and high sintering temperature. Rapid grain growth may have resulted in coarse and porous grain structure [21,22].

Increase in density of the samples from S2 to S6 may be attributed to process (a) due to their small ferrite content. Process (b) dominates for samples S8 and S10, resulting into their low density. Sample S6 possesses highest density as compared to other composite compositions because it has maximum number of pores between BST grains filled by NCF nanoparticles. The role of this process in increasing the density dominates the increase in porosity (because of over sintering of NCF).

2) After filling the maximum number of pores NCF particles have a tendency to segregate together (clearly seen in SEM images of samples S8 and S10) and form cluster leading to increase in porosity in samples S8 and S10.
3) Samples S8 and S10 due to their high ferrite content possess lower density which may be attributed to low density of pure NCF (4.78 g/cm^3) as compared pure BST (5.68 g/cm^3).

Table 1
Crystallographic, structure refinement parameters and density of the composite samples.

Parameter	S0	S2	S4	S6	S8	S10
R_p (%)	18.3	21.5	19.4	20.9	25.7	22.5
R_{wp} (%)	24.7	27.3	25.9	28	33.1	29.1
R_{exp} (%)	14.6	15.78	16.17	15.48	14.50	16.47
χ^2	2.86	3.00	2.56	3.28	5.21	3.12
Lattice parameters (Ferroelectric phase) Å	$a=3.995$	$a=3.999$	$a=3.996$	$a=4.000$	$a=4.007$	$a=3.992$
	$c=4.019$	$c=4.025$	$c=4.020$	$c=4.026$	$c=4.032$	$c=4.015$
	$c/a=1.006$	$c/a=1.006$	$c/a=1.006$	$c/a=1.006$	$c/a=1.006$	$c/a=1.006$
Lattice constant (Ferrite phase) Å	–	8.350	8.343	8.350	8.360	8.336
Experimental density ρ_e (gm/cm^3)	5.68	5.00	5.26	5.68	5.04	4.43
X-ray density ρ_x (gm/cm^3)	5.96	5.95	5.94	5.93	5.91	5.90
Relative density ρ_r (%)	95.00	83.95	88.56	95.84	85.00	75.00
Porosity P (%)	5.00	16.05	11.44	4.16	15.00	25.00
Average grain size (μm)	0.70	0.73	0.74	0.75	0.63	0.62

3.2. Microstructure analysis

Fig. 3(a, b) show TEM images of $Ni_{0.8}Co_{0.2}Fe_2O_4$ and $Ba_{0.95}Sr_{0.05}TiO_3$, respectively. TEM image of NCF shows the particles with nearly spherical shape having sizes in the range 25–60 nm. Fig. 3(b) indicates that BST particles are of irregular shape with size in the micrometer range. NCF prepared by sol–gel method, possesses uniform grain structure (as indicated by SEM image shown in Fig. 4(a)). SEM images of the fractured surface of pure BST and composite samples are shown in Fig. 4(b). Addition of NCF in BST results into irregular grain shape. This may be attributed to the filling of pores between ferroelectric grains by NCF nanoparticles and their segregation at the grain boundaries. The average grain size was calculated using line intercept method and is listed in Table 1. The EDS results for samples S2, S4, S6, S8 and S10 yielded quantitative elemental analysis as shown in Fig. 4(c). Energy spectrum indicates the presence of Ni, Co, Fe, Sr, Ba and O elements. Concentration (wt%) of these elements, as given by the EDS spectrum, matches with composition of the composites. The EDS spectrum was measured at different regions of the composite pellets and it was found that ferroelectric phase is uniformly surrounded by ferromagnetic phase.

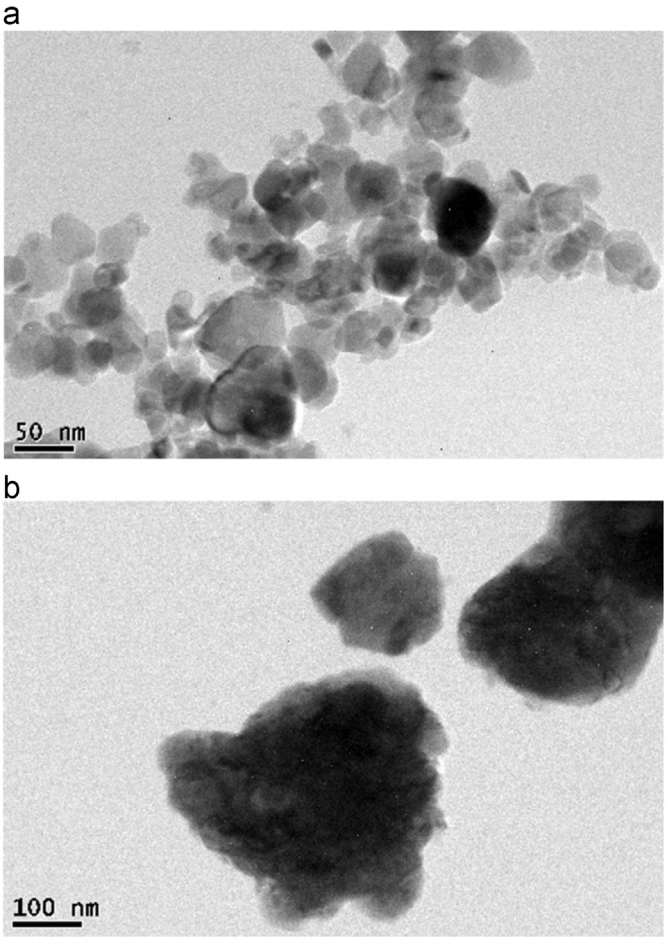

Fig. 3. (a) TEM image of nanoparticles of $Ni_{0.8}Co_{0.2}Fe_2O_4$ after calcination at 950 °C and (b) TEM image of particles of $Ba_{0.95}Sr_{0.05}TiO_3$.

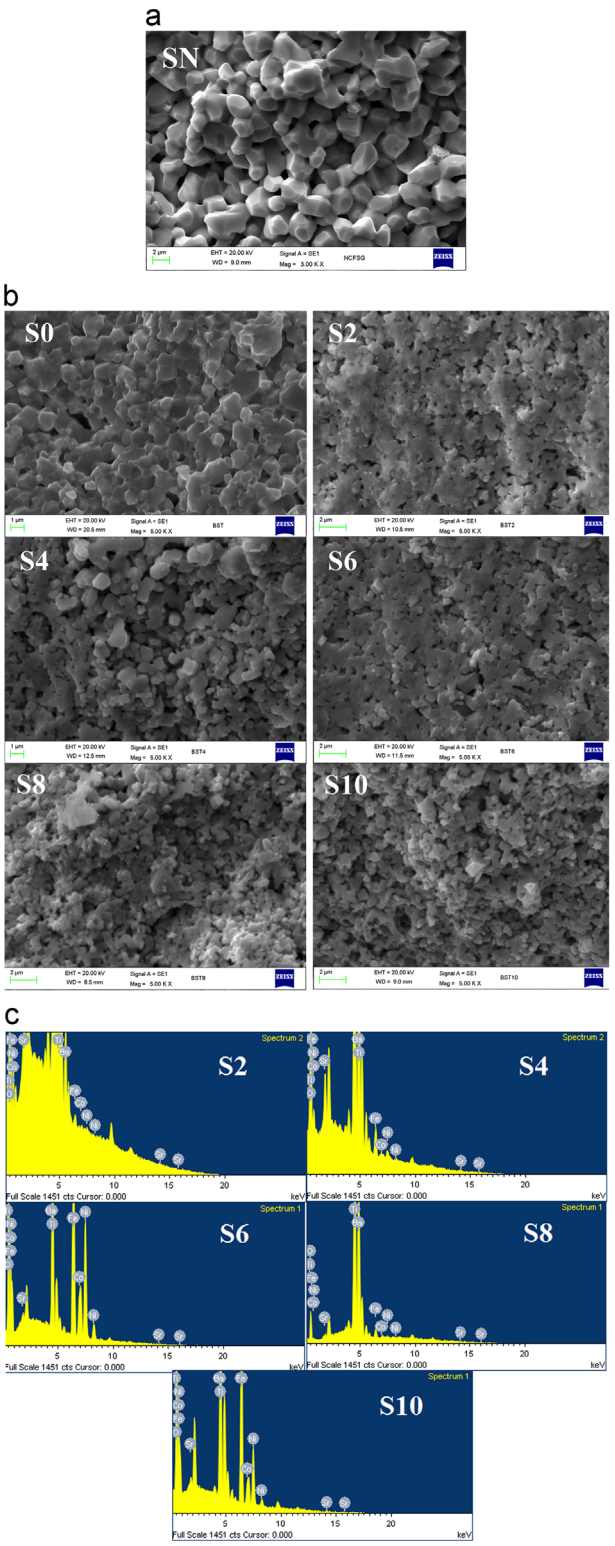

Fig. 4. (a) SEM images of NCF after sintering at 1200 °C. (b) SEM images of pure BST and composite samples after sintering at 1250 °C and (c) EDS spectrum of the composite samples.

3.3. Dielectric properties

Fig. 5(a, b) show the variation of real part of dielectric constant (ε') and dielectric loss ($\tan\delta$) with frequency for

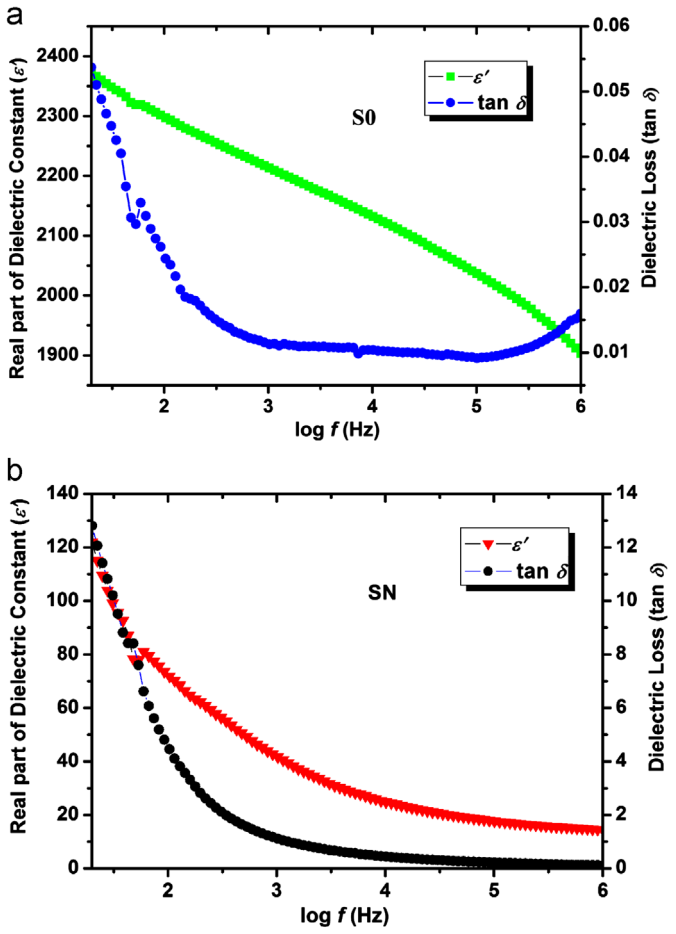

Fig. 5. (a) Variation of real part of dielectric constant (ε') and dielectric loss with frequency for BST. (b) Variation of real part of dielectric constant (ε') and dielectric loss with frequency for NCF.

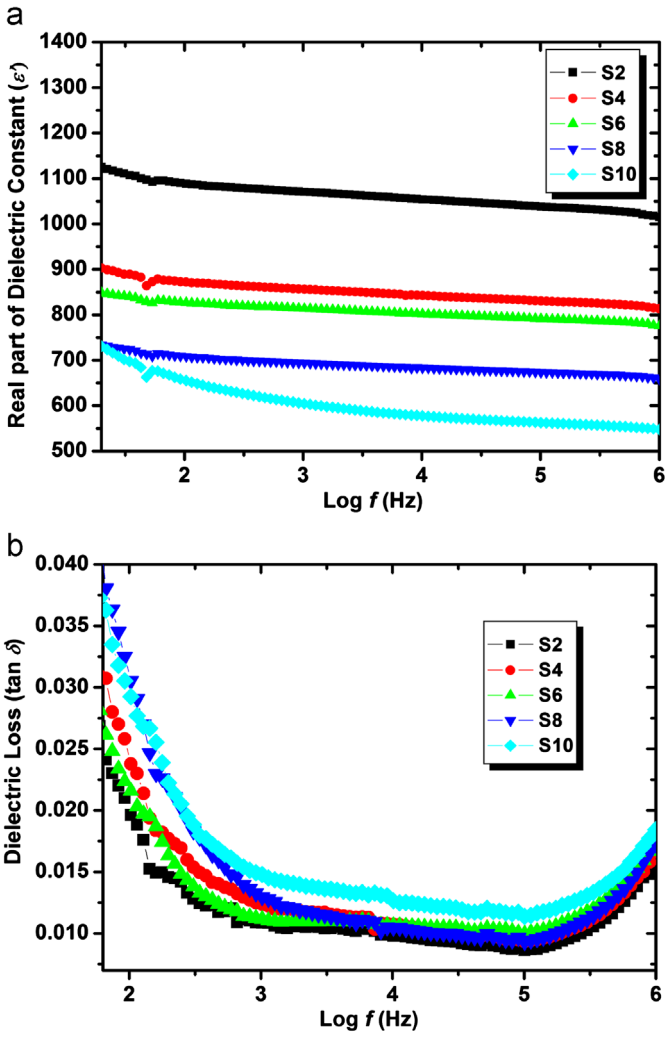

Fig. 6. (a) Variation of real part of dielectric constant (ε') with frequency for the composite samples. (b) Variation of dielectric loss with frequency for the composite samples.

samples S0 and SN, respectively at 30 °C. Fig. 6(a, b) show the variation of real part of dielectric constant (ε') and dielectric loss, respectively with frequency for samples S2, S4, S6, S8, and S10 at 30 °C. Dielectric constant decreases with increase in frequency. It is a usual dielectric dispersion and can be explained in terms of Maxwell–Wagner relaxation mechanism [23–25] which arises at the interface of material with different conductivities due to charge accumulation. In the composites, these types of interfaces arise at the area of contact between ferrite and ferroelectric phases. On the higher frequency side, dominant contribution towards polarization comes from electrical polarization whereas other types of polarizations such as dipolar and interfacial are effective at the lower frequency side. As the frequency increases, charge carriers cannot follow the alternation of electric field and hence dielectric constant decreases. Dielectric constant decreases with increase in ferrite content. This may be attributed to low dielectric constant of NCF as compared to BST. Fig. 6(b) clearly indicates that there is a net increase in dielectric loss of the composite samples with increase in ferrite content. This may be attributed to low resistivity of ferrite phase as compared to ferroelectric phase. NCF particles offer leakage

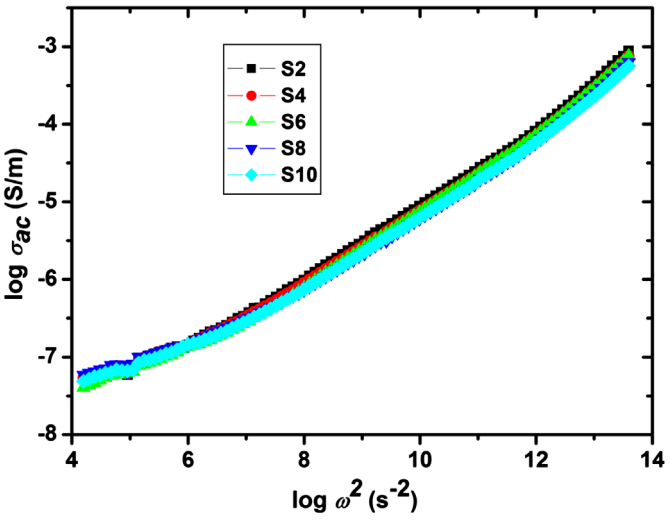

Fig. 7. Variation of log σ_{ac} with log ω^2.

path to charge carriers and hence losses such as conduction losses increase.

3.4. AC conductivity

AC conductivity (σ_{ac}) is an important property of a material which reveals the conduction process involved in the material. AC conductivity was calculated using the relation

$$\sigma_{ac} = 2\pi f \varepsilon_o \varepsilon' \tan\delta \quad (4)$$

where f is the frequency, ε_0 is permittivity of vacuum and ε' is real part of dielectric constant and tan δ is dielectric loss.

In case of conduction by small polaron following relation holds good

$$\sigma_{ac} - \sigma_{dc} = \omega^2\tau^2/(1+\omega^2\tau^2) \quad (5)$$

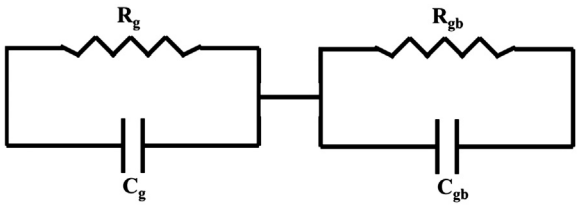

Fig. 8. Equivalent RC circuit exhibiting bulk and grain boundary in composite samples.

where ω is angular frequency, τ is staying time ($\sim 10^{-10}$ s) for frequencies $\omega^2\tau^2$ less than 1. Fig. 7 shows the variation of log σ_{ac} with log ω^2. The plots are nearly straight line thereby confirming that conduction in the composites is due to small polaron [26,27].

3.5. Impedance spectroscopy

Impedance spectrum separates out the grain and grain boundary contribution to electric response for better understanding of material characteristics. Cole–Cole plots consist of real part of impedance (Z') plotted against imaginary part of impedance (Z''). Complex impedance of ME composites ideally can be demonstrated as the sum of two parallel RC circuits connected in series (as shown in Fig. 8), where R_bC_b and $R_{gb}C_{gb}$ networks correspond to the grain and grain boundary contributions, respectively. Typically, Cole–Cole plots for the ME composites are composed of two semicircles [28,29], where each semicircle represents a distinct process with time constant different from the other. The grain and grain boundary contribution dominate at high and low frequencies, respectively.

Fig. 9(a–c) show the Cole–Cole plots of the composite samples S2, S4, S6, S8 and S10 at different temperatures. Plots show two partially superimposed semicircles. Centers of two

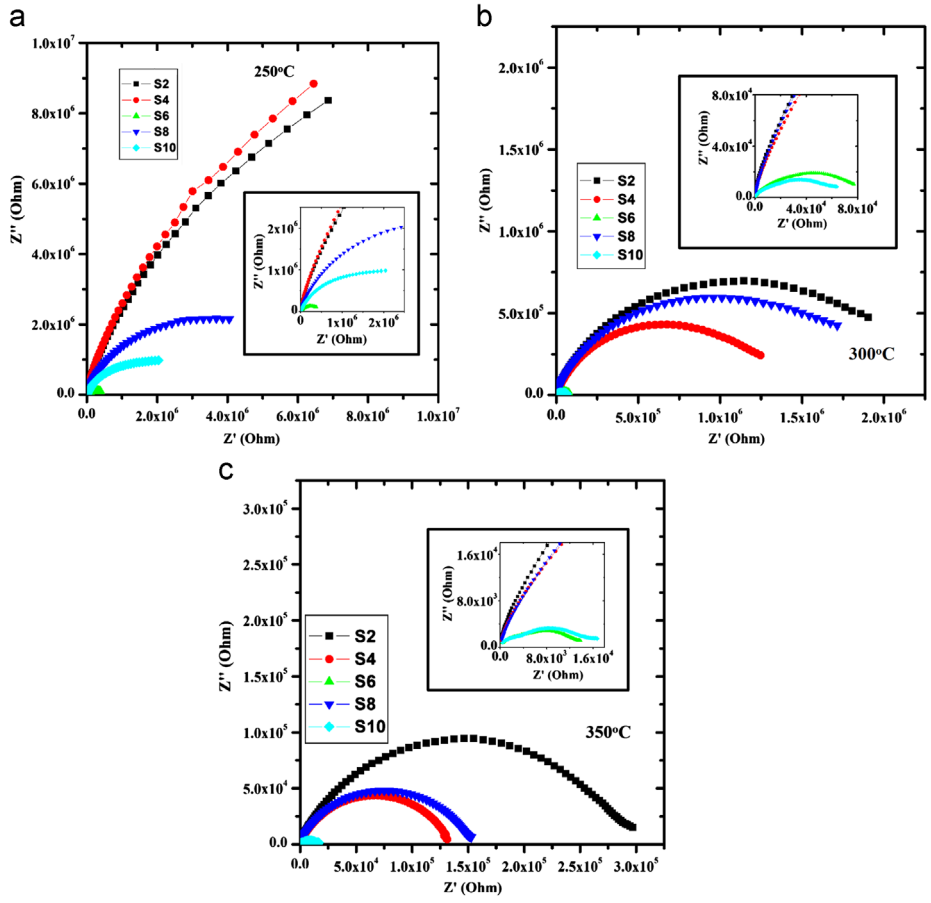

Fig. 9. (a) Cole–Cole plots of the composite samples at 250 °C. (b) Cole–Cole plots of the composite samples at 300 °C. (c) Cole–Cole plots of the composite samples at 350 °C.

semicircles lie below the real axis and very close to each other. Intercept at Z' axis obtained on extrapolation of these semicircles (in Fig. 9(a–c)) gives the approximate value of grain and grain boundary resistance for all the samples at three different temperatures. These values are listed in Table 2. It is clear from Fig. 9 that with increase in temperature resistance of both grain and grain boundary decreases. This is due to generation of more space charge carriers with the rise in temperature, thereby indicating towards semiconducting nature of the composites. There is an overall (although irregular) decrease in resistance of both grain (R_g) and grain boundary (R_{gb}) with increase in ferrite content in the composite samples. This may be attributed to lower resistance of NCF as compared to BST. Such variation in resistance values is consistent with other reports [30]. Large number of factors such as density, oxygen vacancies (developed during high temperature sintering), interfaces between ferrite and ferroelectric phases, resistance of ferrite and ferroelectric phases, etc. are responsible for deciding grain and grain boundary resistance in the composites. This resulted into irregular trend of resistance values. The composite sample S6 abnormally possesses lower value of resistances (R_g, R_{gb}) as compared to samples S8 and S10, which may be attributed to its high density.

3.6. Ferroelectric properties

Ferroelectric properties of the multiferroic composites were determined by measuring polarization vs. electric field (P–E) characteristics. These characteristics yield useful information regarding its electrical structure i.e. dipoles and their response in the presence of alternating field. Fig. 10 shows the P–E loops of the composites measured using Sawyer–Tower circuit at 50 Hz and corresponding to a temperature of 30 °C. The values of remanant polarization (P_r), saturation polarization (P_s) and coercive field (E_c) are listed in Table 3. P–E loops of the composite samples are unsaturated. There is a significant decrease in values of saturation and remanant polarization in the composite samples as compared to pure BST. These two factors clearly point towards dilution of ferroelectric properties of BST ceramics on addition nanoparticles of NCF. Decrease in P_r and P_s values in the composite samples as compared to pure BST may be attributed to

1) Low resistance of NCF resulting in lower undertaking electrical voltage, so that the composite samples may not get fully polarized [31].
2) Increase in dielectric loss with the addition of ferrite material.
3) Segregation of NCF nanoparticles along BST grain boundaries which increases percolation path for charge carriers [32].
4) Interfacial polarization and heterogeneous conduction between ferrite and ferroelectric interfaces [12].

Sample S10 possesses the highest value of coercive field. There is significant rise in coercive field with increase in ferrite content. This indicates that motion of the domain wall of the ferroelectric regions becomes difficult as ferrite content increases [33,34]. Further P–E loops of the composites are unsymmetrical about origin. This may be due to internal bias field caused by defects [35] and short distance, off center, inherent movement of bound electrons [34].

3.7. Magnetic properties

The magnetic properties of the material were characterized by its magnetization vs. magnetic field (M–H) measurements which indicate the behavior of the material when excited in an external magnetic field. Fig. 11 shows M–H loops of the composite samples at 30 °C. The values of various magnetic parameters are listed in Table 4. All samples show well

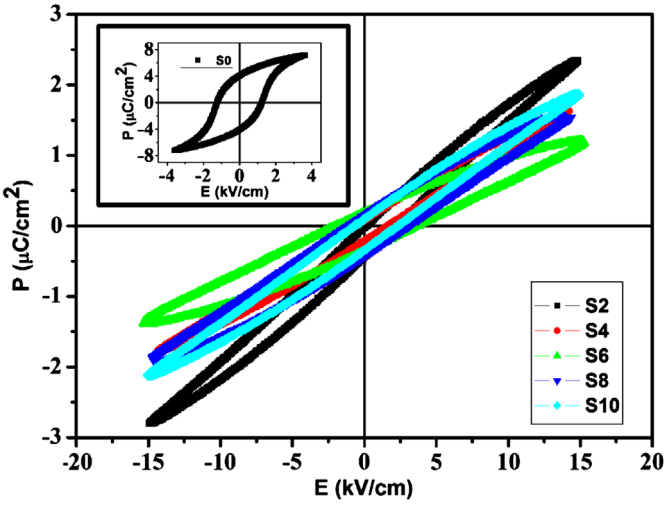

Fig. 10. Polarization vs. electric field (P–E) loop of the composites with inset showing the P–E loop of pure $Ba_{0.95}Sr_{0.05}TiO_3$.

Table 2
Grain resistance (R_g) and Grain boundary resistance (R_{gb}) for the composites S2, S4, S6, S8, and S10 at 250 °C, 300 °C, and 350 °C.

Composition	At 250 °C		At 300 °C		At 350 °C	
	R_g (kΩ)	R_{gb} (kΩ)	R_g (kΩ)	R_{gb} (kΩ)	R_g (kΩ)	R_{gb} (kΩ)
S2	282000	340800	2042	2281	283	296
S4	238500	333900	1281	1464	132	135
S6	370	480	65	84	10	13
S8	4900	6660	1452	2093	150	153
S10	2119	3641	545	679	11	15

saturated hysteresis loops indicating the presence of ordered magnetic structure in the composites [36]. It is clearly seen in Table 4 that all the composite samples possess smaller values of remanant and saturation magnetization as compared to pure NCF because of their much lower ferrite content. The values of remanant and saturation magnetization of the composite increase with increase in ferrite content. Exchange interaction between neighboring uncompensated spins is the basic requirement for a material to be ferromagnetic. Non-magnetic BST particles act like pores between ferrite particles. They break the exchange interaction resulting into dilution of ferromagnetic properties of the composites. The composite samples possess high values of coercive field as compared to pure NCF. The magnetization in the composites is hard to realize. The multiferroic composite possess high value of reduced magnetization (M_r/M_s) as compared with pure $Ni_{0.8}Co_{0.2}Fe_2O_4$. Reduced magnetization is also called squareness of hysteresis loop. It has values lying in range 0–1 and is a measure of application of material in memory devices [37]. Hence these composites can potentially be used in memory devices.

Table 3
Variation of remanant polarization (P_r), Saturation polarization (P_s) and Coercive field (E_c) of the composite samples.

Composition	P_r (μC/cm^2)	P_s (μC/cm^2)	E_c (kV/cm)
S0	4.084	7.190	1.242
S2	0.207	2.574	1.075
S4	0.151	1.704	1.121
S6	0.278	1.302	2.869
S8	0.280	1.758	2.032
S10	0.219	1.998	4.446

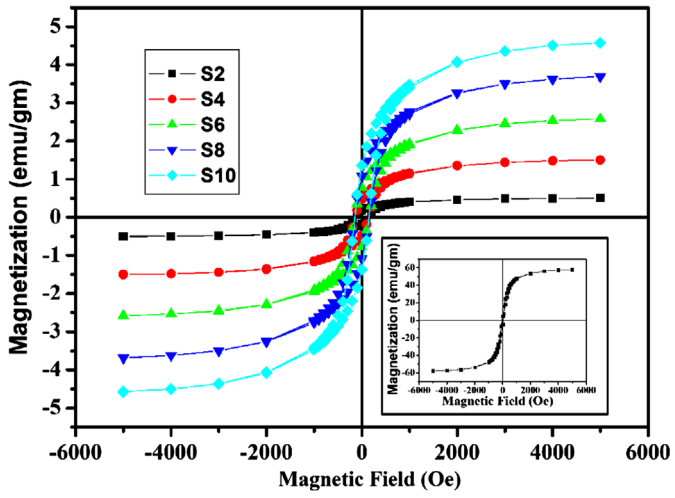

Fig. 11. Magnetization vs. Magnetic Field (M–H) characteristics of the composites with inset showing M–H loop of pure $Ni_{0.8}Co_{0.2}Fe_2O_4$.

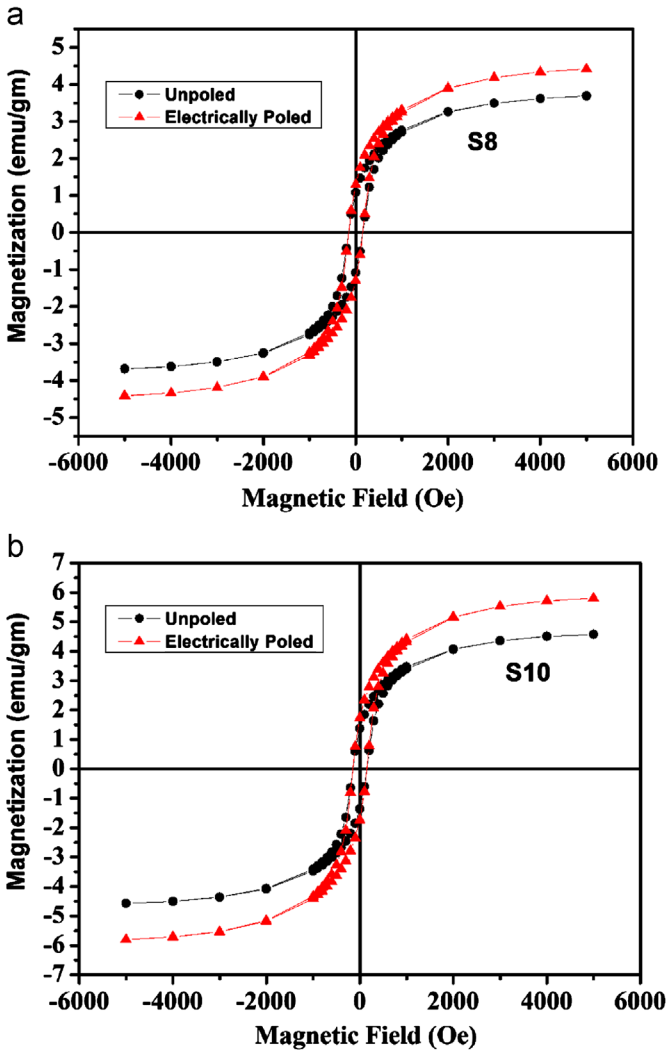

Fig. 12. (a) Magnetic hysteresis loops of both electrically poled and unpoled samples for the composite S8. (b) Magnetic hysteresis loops of both electrically poled and unpoled samples for the composite S10.

Table 4
Magnetic Parameters of the composite samples.

Composition	Remanant magnetization (M_r) (emu/gm)	Saturation magnetization (M_s) (emu/gm)	M_r/M_s	Coercive field (H_c) (Oe)
SN	4.540	31.847	0.143	41.136
S2	0.1898	0.2787	0.681	146.53
S4	0.4639	0.7446	0.623	139.27
S6	0.8379	1.3216	0.634	150.49
S8	1.147	1.847	0.621	153.01
S10	1.378	2.237	0.616	147.43

Table 5
Magnetic Parameters of electrically poled and unpoled pellets for sample S8 and S10.

Composition	State	Remanant magnetization (M_r) (emu/gm)	Saturation magnetization (M_s) (emu/gm)	Coercive field (H_C) (Oe)
S8	Electrically poled	1.28	3.96	152
S8	Electrically unpoled	1.07	3.08	152
% Change		19.62	28.57	–
S10	Electrically poled	1.72	5.26	147
S10	Electrically unpoled	1.35	4.10	147
% Change		27.40	28.29	–

3.8. Magnetoelectric properties

Nanoparticles of $Ni_{0.8}Co_{0.2}Fe_2O_4$ have high specific surface area which results in better *M–E* coupling [38]. To confirm magnetoelectric coupling between ferroelectric and ferrite phases, two pieces from a single pellet were taken, one of them was electrically poled at 5 kV/mm and the other was unpoled. *M–H* hysteresis loop of both poled and unpoled samples were taken using VSM. Fig. 12(a, b) show hysteresis loop of both poled and unpoled pieces for the samples S8 and S10, respectively. Parameters obtained from magnetic measurements are listed in Table 5. Similar results have been recorded by many research groups [39,40]. Significant increase in both saturation and remanant magnetization of electrically poled samples indicates strong magnetoelectric coupling between two constituents. This increase in magnetization values of electrically poled samples may be attributed to poling of sample which may result into aligning of individual dipole-moments within different electric domains along the electric field direction. As magnetoelectric coupling is related to elastic interaction of ferroelectric and ferromagnetic domains [41], movement of electrical domain walls alters local strain which results in change in magnetic anisotropy and hence corresponding increase in magnetization [7].

4. Conclusion

XRD patterns of NCF–BST composite system confirmed the formation of cubic spinel and perovskite structure of NCF and BST, respectively. The composite samples show dielectric dispersion at low frequency due to Maxwell–Wagner relaxation mechanism. Dielectric constant of the composite samples decreases with increase in ferrite content. Grain and grain boundary resistance decreases with increase in ferrite content. Addition of ferrite in ferroelectric material results in enhanced coercive field of *P–E* loop in the composites. With increase in ferrite content the remanant magnetization (M_r) and saturation magnetization (M_s) of *M–H* loop increases. The significant increase in M_r/M_s values of composite samples as compared to NCF increases the possibility of use of these composites in memory based applications. Enhancement in magnetization values in *M–H* loop of electrically poled and unpoled samples confirmed magnetoelectric coupling between ferrite and ferroelectric phases.

Acknowledgment

One of the authors (Poonam Pahuja) would like to thank Department of Science and Technology (DST), Government of India, for awarding INSPIRE Fellowship and Dr. N.C. Mehra (University of Delhi, New Delhi) for helping in SEM measurements.

References

[1] Jing Ma, Jiamian Hu, Zheng Li, Ce-Wen Nan, Recent progress in multiferroic magnetoelectric composites: from bulk to thin films, Advanced Materials 23 (2011) 1062–1087.
[2] Silvia Picozzi, Claude Ederer, First principles studies of multiferroic materials, Journal of Physics: Condensed Matter 21 (2009) 303201.
[3] L.W. Martin, S.P. Crane, Y.-H. Chu, M.B. Holcomb, M. Gajek, M. Huijben, C.-H. Yang, N. Balke, R. Ramesh, Multiferroic and magnetoelectrics: thin films and nanosturctures, Journal of Physics: Condensed Matter 20 (2008) 434220.
[4] Rahul C. Kambale, Dae-Yong Jeong, Jungho Ryu, Current status of manetoelectric composite thin/thick films, Advances in Condensed Matter Physics 2012 (2012) 1–15 824643.
[5] Shashank Priya, Rashed Islam, Shuxiang Dong, D. Viehland, Recent advancements in magnetoelectric particulate and laminate composites, Journal of Electroceramics 19 (2007) 147–164.
[6] Subhasis Roy, S.B. Majumder, Recent advances in multiferroic thin films and composites, Journal of Alloys and Compounds 538 (2012) 153–159.
[7] Ce-Wen Nan, M.I. Bichurin, Shuxiang Dong, D. Viehland, G. Srinivasan, Multiferroic magnetoelectric composites: historical perspective, status, and future directions, Journal of Applied Physics 103 (2008) 031101.
[8] Yao Wang, Jiamian Hu, Yuanhua Lin, Ce-Wen Nan, Multiferroic magnetoelectric composite nanostructures, NPG Asia Materials 2 (2) (2010) 61–68.
[9] Daniel Khomskii, Classifying multiferroics: mechanisms and effects, Physics 2 (2009) 20.
[10] R. Balachandran, B.H. Ong, H.Y. Wong, K.B. Tan, M. Muhamad Rasat, Dielectric characteristics of barium strontium titanate based metal insulator metal capacitor for dynamic random access memory cell, International Journal of Electrochemical Science 7 (2012) 11895–11903.
[11] Jing Jiang, A facile method to the $Ni_{0.8}Co_{0.2}Fe_2O_4$ nanocrystalline via a refluxing route in ethylene glycol, Materials Letters 61 (2007) 3239–3242.
[12] Renbing Sun, Bijun Fang, Qingbo Du, Huiqin Zhang, Xiangyong Zhao, Haosu Luo, Microstructural, electrical and magnetoelectric properties of low-temperature sintering $(Ni_{0.8}Zn_{0.1}Cu_{0.1})Fe_2O_4$/[0.48 PNN–0.02 PZN–0.05 PNW–0.45 PT] composites, Smart Materials and Structures 19 (2010) 035026.
[13] Gary Evans, Giap V. Duong, Michael J. Ingleson, Zhongling Xu, James T.A. Jones, Yaroslav Z. Khimyak, John B. Claridge, Matthew J. Rosseinsky, Chemical bonding assembly of multifunctional oxide nanocomposites, Advanced Functional Materials 20 (2010) 231–238.

[14] Carlos A.F. Vaz, Jason Hoffman, Charles H. Ahn, Ramamoorthy Ramesh, Magnetoelectric coupling effects in multiferroic complex oxide composite structures, Advanced Materials 22 (2010) 2900–2918.
[15] L.V. Leonel, A. Righi, W.N. Mussel, J.B. Silva, N.D.S. Mohallem, Structural characterization of barium titanate-cobalt ferrite composite powders, Ceramics International 37 (2011) 1259–1264.
[16] Lawrence Kumar, Manoranjan Kar, Effect of La^{3+} substitution on the structural and magnetocrystalline anisotropy of nanocrystalline cobalt ferrite ($CoFe_{2-x}La_xO_4$), Ceramics International 38 (2012) 4771–4782.
[17] S. Ghatak, M. Sinha, A.K. Meikap, S.K. Pradhan, Anomalous electrical transport properties of nonstoichiometric nickel ferrite below room temperature, Materials Research Bulletin 46 (2011) 1055–1064.
[18] Kavita Verma, Ashwini Kumar, Dinesh Varshney, Dielectric relaxation behavior of $A_xCo_{1-x}Fe_2O_4$ (A=Zn, Mg) mixed ferrites, Journal of Alloys and Compounds 526 (2012) 91–97.
[19] R. Mukherjee, T. Sahu, S. Sen, P. Sahu, Structural and microstructural evolution due to increasing Co substitution in $Ni_{1-x}Co_xFe_2O_4$: an X-ray diffraction study using the Rietveld method, Materials Chemistry and Physics 128 (2011) 365–370.
[20] A.A. Kadam, S.S. Shinde, S.P. Yadav, P.S. Patil, K.Y. Rajpure, Structural, morphological, electrical and magnetic properties of Dy doped Ni–Co substitutional spinel ferrite, Journal of Magnetism and Magnetic Materials 329 (2013) 59–64.
[21] C. Miclea, C. Tanasoiu, I. Spanulescu, C.F. Miclea, A. Gheorghiu, L. Amarande, M. Cloangher, C.T. Miclea, Microstructure and properties of barium titanate ceramics prepared by mechanochemical synthesis, Romanian Journal of Information Science and Technology 10 (4) (2007) 335–345.
[22] S.T. Mahmud, A.K.M. Akther Hossain, A.K.M. Abdul Hakim, M. Seki, T. Kawai, H. Tabata, Influence of microstructure on the complex permeability of spinel type Ni–Zn ferrite, Journal of Magnetism and Magnetic Materials 305 (2006) 269–274.
[23] Ravindar Tadi, Yong-II Kim, Kwon-Sang Ryu, CheolGi Kim, Effect of magnetic field on the dielectric properties of multiferroic composites, Journal of the Korean Physical Society 61 (9) (2012) 1545–1549.
[24] J.C. Maxwell, Electricity and Magnetism, Oxford University Press, London, 1973.
[25] C.M. Kanamadi, J.S. Kim, H.K. Yang, B.K. Moon, B.C. Choi, J. H. Jeong, Synthesis and characterization of $CoFe_2O_4$–$Ba_{0.9}Sr_{0.1}TiO_3$ magnetoelectric composites with dielectric and magnetic properties, Applied Physics A 97 (2009) 575–580.
[26] S.A. Lokare, R.S. Devan, D.R. Patil, B.K. Chougule, Studies on electrical properties of (x) $BaTiO_3$+(1−x) $Ni_{0.92}Co_{0.03}Mn_{0.05}Fe_2O_4$ ME composites, Journal of Materials Science: Materials in Electronics 18 (2007) 1211–1215.
[27] R.C. Kambale, P.A. Shaikh, C.H. Bhosale, K.Y. Rajpure, Y.D. Kolekar, Dielectric properties and complex impedance spectroscopy studies of mixed Ni–Co ferrites, Smart Materials and Structures 18 (2009) 085014.
[28] Zhi Yu, Chen Ang, Maxwell–Wagner polarization in ceramic composites $BaTiO_3$–$(Ni_{0.3}Zn_{0.7})Fe_{2.1}O_4$, Journal of Applied Physics 91 (2002) 794.
[29] N. Ortega, Ashok Kumar, P. Bhattacharya, S.B. Majumder, R.S. Katiyar, Impedance spectroscopy of multiferroic $PbZr_xTi_{1-x}O_3$/$CoFe_2O_4$ layered thin films, Physical Review B 77 (2008) 014111.
[30] D.K. Pradhan, R.N.P. Chowdhary, T.K. Nath, Magnetoelectric properties of $PbZr_{0.53}Ti_{0.47}O_3$–$Ni_{0.65}Zn_{0.35}Fe_2O_4$ multiferroic nanocomposites, Applied Nanoscience 2 (2012) 261–273.
[31] Arif D. Sheikh, V.L. Mathe, Dielectric, ferroelectric, magnetic and magnetoelectric properties of PMT-PT based ME composites, Journal of Physics and Chemistry of Solids 72 (2011) 1423–1429.
[32] Ashi Ofir, Snir Dor, Larisa Grinis, Arie Zaban, Thomas Ditrich, Juan Bisquert, Porosity dependence of electron percolation in nanoporous TiO_2 layers, Journal of Chemical Physics 128 (2008) 064703.
[33] Wang Ye-An, Wang Yun-Bo, Rao Wei, Gao Jun-Xiong, Zhou Wen-Li, Yu Jun, Electric and magnetic properties of the (1−x) $Ba_{0.6}Sr_{0.4}TiO_3$–$CoFe_2O_4$ multiferroic composite ceramics, Chinese Physics Letters 29 (6) (2012) 067701.
[34] XiWei Qi, Ji Zhou, Baorang Li, Yingchun Zhang, Zhenxing Yue, Zhilun Gui, Longtu Li, Preparation and spontaneous polarization–magnetization of a new ceramic ferroelectric–ferromagnetic composites, Journal of the American Ceramic Society 87 (10) (2004) 1848–1852.
[35] Yanxi Li, Yaodong Yang, Jianjun Yao, Ravindranath Viswan, Zhiuing Wang, Controlled growth of epitaxial $BiFeO_3$ films using self-assembled $BiFeO_3$–$CoFe_2O_4$ multiferroic hetrostructures as a template, Applied Physics Letters 101 (2012) 022905.
[36] L. Mitoseriu, I. Pallecchi, V. Buscaglia, A. Testino, C.E. Ciomaga, A. Stancu, Magnetic properties of the $BaTiO_3$–(NiZn)Fe_2O_4 multiferroic composites, Journal of Magnetism and Magnetic Materials 316 (2007) e603–e606.
[37] Abdulhadi Baykal, Nermin Kasapoglu, Zehra Durmus, Huseyin Kavas, Muhammet S. Toprak, Yuksel Koseoglu, CTAB-assisted hydrothermal synthesis and magnetic characterization of $Ni_xCo_{1-x}Fe_2O_4$ nanoparticles, Turkish Journal of Chemistry 33 (2009) 33–45.
[38] V.M. Laletin, V.V. Pan'kov, Influence of powder surface area on the manetoelectric effect in barium lead zirconatetitanate/nickel ferrite composite ceramics, Inorganic Materials 48 (2012) 87–92.
[39] Rekha Rani, J.K. Juneja, Sangeeta Singh, K.K. Raina, Chandra Prakash, Study of 0.1 $Ni_{0.8}Zn_{0.2}Fe_2O_4$–0.9$Pb_{1-3x/2}La_xZr_{0.65}Ti_{0.35}O_3$, Journal of Magnetism and Magnetic Materials 325 (2013) 47–51.
[40] Anupinder Singh, Ishan Choudhary, Sunita Mehta, Sajjan Dahiya, Chitsimranjit Singhwalia, K.K. Raina, Ratnamala Chatterjee, Optimal multiferroic properties and enhanced magnetoelectric coupling in $SmFeO_3$–$PbTiO_3$ solid solution, Journal of Applied Physics 107 (2010) 084106.
[41] J. Kulawik, D. Szwagier, P. Guzdik, Magnetic, magnetoelectric and dielectric behavior of $CoFe_2O_4$–$Pb(Fe_{1/2}Nb_{1/2})O_3$ particulate and layered composites, Journal of Magnetism and Magnetic Materials 324 (2012) 3052–3057.